PHYSICAL REVIEW B **68**, 024512 (2003)

Dzialoshinskii-Moriya interaction in the organic superconductor κ-$(\mathrm{BEDT\text{-}TTF})_2\mathrm{Cu}[\mathrm{N(CN)}_2]\mathrm{Cl}$

Dylan F. Smith,* Stewart M. De Soto,† and Charles P. Slichter
Department of Physics, University of Illinois at Urbana-Champaign, Urbana, Illinois 61801, USA

John A. Schlueter, Aravinda M. Kini, and Roxanne G. Daugherty
Materials Science Division, Argonne National Laboratory, Argonne, Illinois 60439, USA

(Received 11 February 2003; published 23 July 2003)

The authors report ^{13}C NMR and magnetization measurements on the magnetic state of oriented single crystals of the organic superconductor κ-(BEDT-TTF)$_2$Cu[N(CN)$_2$]Cl. To understand these data a spin Hamiltonian based on the *Pnma* symmetry of the crystal is developed. When interpreted in the context of this Hamiltonian, the measurements provide a detailed picture of the spin ordering. It is found that the Dzialoshinskii-Moriya (DM) interaction is largely responsible for the details of the ordering above the spin-flop field. Of particular note, the interplane correlations are determined by the intraplane DM interactions and the direction of the applied field.

DOI: 10.1103/PhysRevB.68.024512 PACS number(s): 74.70.Kn, 75.25.+z, 75.50.Ee, 76.60.Jx

I. INTRODUCTION

Much work has gone into understanding the magnetic and superconducting properties of κ-(BEDT-TTF)$_2$Cu[N(CN)$_2$]X (X=Br,Cl,I) (Refs. 1–3) and related systems of quasi-two-dimensional organic conductors. These systems consist of insulating layers of polymers alternating with conducting layers of dimers of the BEDT-TTF molecule [BEDT-TTF, hereafter abbreviated as ET, is bis(ethylenedithio)tetrathiafulvalene]. While the nature of the superconducting state has been disputed (see, e.g., Refs. 4 and 5), many researchers have suggested on the basis of experiment that the order parameter is anisotropic with nodes in the gap, and comparisons to the high-T_C superconductors have been made.[6–8] The interplay between superconductivity and antiferromagnetism in these systems is of particular interest, as antiferromagnetic spin fluctuations have been proposed as a mechanism for the superconductivity.[9–12] A thorough characterization of the magnetic state may provide a basis on which to develop such theories. While the presence of antiferromagnetic fluctuations is seen in several of the κ-(ET)$_2$Cu[N(CN)$_2$]X compounds, two that exhibit antiferromagnetic ordering are the X=Cl salt and the deuterated X=Br (d-Br) salt. In this paper, we use a combination of NMR and magnetization measurements to find the magnetic structure of the X=Cl salt and show the key role of the Dzialoshinskii-Moriya (DM) interaction[13–15] in producing the magnetic structure.

The Cl salt is an ambient-pressure antiferromagnet with a Néel temperature of 27 K (under pressure, however, it becomes a superconductor[2]). The initial magnetization study of Welp *et al.*[16] identified the antiferromagnetic nature and detected the presence of weak ferromagnetic canting. The subsequent magnetization and ^{1}H NMR data of Miyagawa *et al.*[17] determined T_N to be 27 K, identified an easy axis along $\hat{b}$ through the presence of a spin-flop transition at approximately 0.3 T, and suggested that the ordering was commensurate with the dimer structure.

Further experiments on the magnetic ordering of the Cl and d-Br salts have generally upheld the picture proposed by Miyagawa *et al.* The torque magnetometry data of Pinterić *et al.*[18] confirmed that the easy axis was along $\hat{b}$ and noted that in low fields the weak ferromagnetic canting away from the easy axis was toward $\hat{c}$ and not $\hat{a}$. Later ^{13}C experiments of Miyagawa, Kawamoto, and Kanoda[19,20] on the d-Br salt again found commensurate ordering and identified some constraints on the high-field ordering of the electronic spins when the external field is applied along the $\hat{a}$ axis.

The recent antiferromagnetic resonance (AFMR) experiments of Ohta *et al.*[21] and Ito *et al.*[22] have suggested slightly different configurations for the magnetic ordering in the Cl salt. Instead of an easy axis along $\hat{b}$, Ohta *et al.* found easy-plane anisotropy with an easy plane that was tilted 35° from the $\hat{a}$-$\hat{c}$ plane. Ito *et al.* were not able to fit their angle-dependent AFMR data for the Cl salt to the standard theory, and they interpret their d-Br data as showing the easy axis to be $\hat{a}$.

In this paper we provide a microscopic framework for understanding our data and show that it helps to explain the results of these previous experiments.

II. EXPERIMENT

A. NMR

For the NMR data a 0.78-mg single-crystal sample of κ-(^{13}C$_2$-ET)$_2$Cu[N(CN)$_2$]Cl was used.[23] This sample is labeled with ^{13}C isotopes at the two ‘‘central’’ carbons of the ET molecule, as explained by De Soto *et al.*[24] The central carbons are located in the region of highest density for the conduction band electrons. The data presented here were taken in superconducting magnets with fields of 8.3 and 11.74 T. A Macor sample mount was used. The spectra were obtained with the spin-echo pulse sequence. Further details can be found in Ref. 24.

B. Magnetometry

The high-field magnetization data were taken on a 16.1-mg single crystal of κ-($^{13}C_6$-ET)$_2$Cu[N(CN)$_2$]Cl.[25] The measurements were made with a Quantum Design Magnetic Property Measurement System (MPMS) magnetometer, which uses a second-order gradiometer superconducting detection coil. The field range was from -7 to $+7$ T at a temperature of 5 K, well below the transition temperature of $T_N = 27$ K. The sample holder was a plastic drinking straw with a Mylar strip inserted.

III. RESULTS

A. NMR

As explained in De Soto *et al.*,[24] when at room temperature with an arbitrary orientation of the external field, a κ-($^{13}C_2$-ET)$_2$Cu[N(CN)$_2$]Cl sample will produce 16 different ^{13}C resonance lines. These 16 lines arise from three sources of splitting. First, the manner in which the dimers form causes the two central carbons in a given molecule to exist in slightly different chemical environments. We call these two distinct sites the inner and outer sites, and they provide a factor of 2 in the number of lines. Second, the four inequivalent dimer orientations in a unit cell lend a factor of 4 to the number of lines. Third, a nuclear dipolar splitting between the two central ^{13}C nuclei provides a factor of 2. Following De Soto *et al.*, we measured the room-temperature ^{13}C Knight- (spin-) shift tensor from an angular study of the resonance line positions in the 11.74-T magnet and found the following:

	K_{xx}^{spin}	K_{yy}^{spin}	K_{zz}^{spin}	α
Inner	-70 ± 20	-141 ± 20	419 ± 20	$7.9°\pm0.8°$
Outer	51 ± 10	-18 ± 10	704 ± 10	$-0.9°\pm0.1°$

where α is the angle by which the principle axes of the hyperfine tensor deviate from the molecular axes and the shifts are given in parts per million (ppm). These results are quite similar to those for the Br salt, which is not surprising, as the structural differences between the Cl and Br salts are minute.

The resonance frequency of the outer ^{13}C site is shown as a function of temperature in Fig. 1 for three orientations of the external field at 8.3 T.[26] The corresponding data for the inner site are shown in Fig. 2. Note that while the shifts of the resonance lines described above are present above T_N, their differences are imperceptible on the scale of the plot.

The significant features of these data are the large shifts at low temperatures with onset near T_N and the lack of any splitting at low temperatures save for the splitting between the inner and outer ^{13}C. The latter is remarkable, as additional splittings from the four inequivalent sites would be expected for arbitrary orientations of the antiferromagnetic sublattice moments. The absence of this splitting in the magnetic state puts stringent constraints on the electron spin ordering, as discussed later.

An additional property of the frequency shifts that is not shown in these data is that, although above T_N the shifts are proportional to the applied field, we have found that below T_N the shifts are largely independent of the applied field for fields ranging from 9.4 T down to 2 T. This reinforces the interpretation of the shifts as arising from spontaneous magnetic ordering. Also, we find spin-lattice relaxation results that are similar to those reported by Kawamoto *et al.*,[27] including a peak in the relaxation rate near T_N.

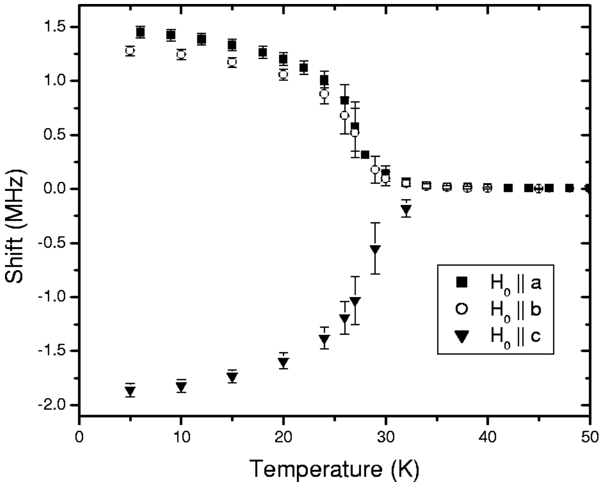

FIG. 1. Resonance frequency of the outer line of the central ^{13}C as a function of temperature at 8.3 T. The error bars represent the linewidth.

B. Magnetometry

Our low-field data ($H<1$ T) for the magnetization as a function of applied field, though not included in this paper, are consistent with the data of Miyagawa *et al.*,[17] including a spin-flop transition at 0.25 T for $\mathbf{H}\|\hat{b}$. In Fig. 3 we present magnetization data for fields up to 7 T for the field along each of the crystal axes. The background magnetization $M_{background}$ was found by measuring in the absence of the sample. The data shown are just the spin magnetic moment of the sample, $M_{spin} = M_{measured} - M_{background} - M_{core}$.

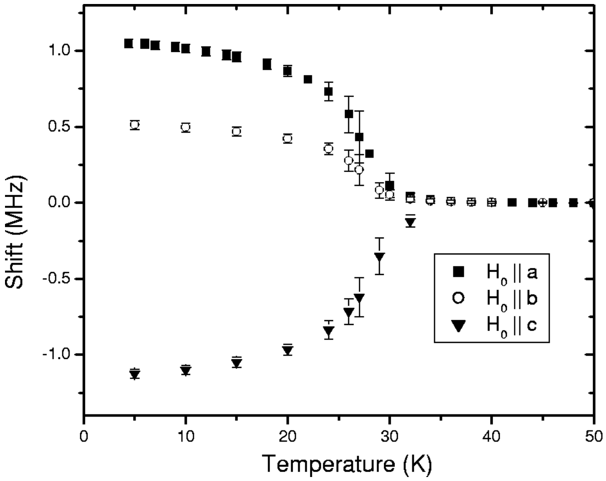

FIG. 2. Resonance frequency of the inner line of the central ^{13}C as a function of temperature at 8.3 T. The error bars represent the linewidth.

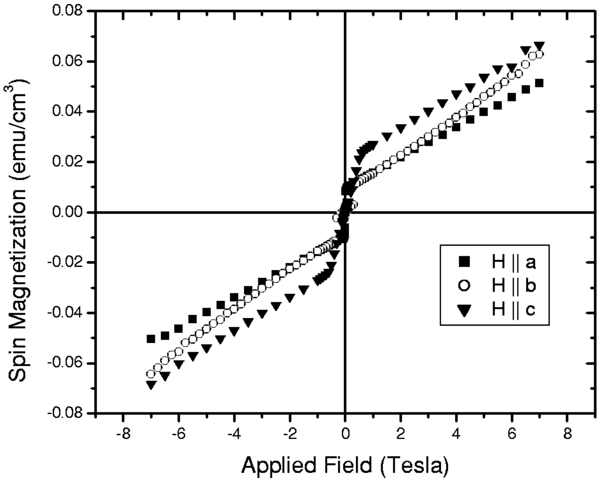

FIG. 3. Spin magnetization as a function of field, $T = 5$ K.

Following Welp *et al.*[16] we use a diamagnetic core contribution of $\chi_{core} = -9.1\times10^{-7}$ emu/cm^3.

IV. DISCUSSION

A. Crystal structure and symmetries

Our analysis of the system relies on knowledge of the symmetries of the crystal. Figure 4 shows several dimer sites in two adjoining layers.

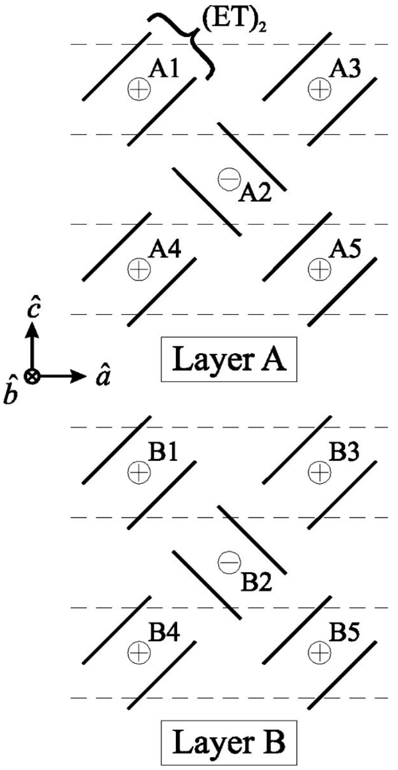

FIG. 4. A schematic diagram showing various sites in two adjacent layers. The pairs of dark lines represent the (ET)$_2$ dimers, the circles represent the electron spins, the + and − labels represent the two magnetic sublattices, and the dashed lines represent the planes of glide symmetry.

There are four inequivalent dimer sites in the unit cell: A1 and A2 in layer A and B1 and B2 in layer B. The space group of the crystal is *Pnma*, which gives us the symmetry operations that describe how these sites are related.[28] The first symmetry operation is a glide $\hat{\mathcal{G}}$, which involves a reflection across the $\hat{a}$-$\hat{b}$ plane and a translation of $\frac{1}{2}$ the unit cell along $\hat{a}$. This operation takes one dimer site in a given layer into the other dimer site, e.g., A1→A2, A2→A3. In Fig. 4 the glide planes are represented by the dashed lines. The other two symmetry operations are a reflection across the $\hat{a}$-$\hat{c}$ plane, $\hat{\mathcal{R}}$, and a diagonal glide in the $\hat{b}$-$\hat{c}$ plane, $\hat{\mathcal{D}}$. Here $\hat{\mathcal{R}}$ takes a site in one layer into the corresponding site in the other layer, e.g., A1→B1. $\hat{\mathcal{D}}$ is a composition of $\hat{\mathcal{G}}$ and $\hat{\mathcal{R}}$ and so will be ignored. There is also an inversion operator $\hat{\mathcal{I}}$, which arises because the dimers are centrosymmetric.

B. Electron spin ordering

The absence of any further splittings of the resonance frequency lines in the magnetic state constrains the possible orderings that we should consider. These constraints are found through analysis of the nuclear spin Hamiltonian, which in the antiferromagnetic state is dominated by the Zeeman and nuclear-electron spin interactions. Here we present the nuclear spin Hamiltonian for a given site i,

$$\begin{aligned}\mathcal{H}_i &= \mathcal{H}_{Zeeman,i} + \mathcal{H}_{spin,i}\\ &= -\gamma_n\hbar\hat{\mathbf{I}}_i\cdot\mathbf{H}_0 + \hat{\mathbf{I}}_i\cdot\mathsf{A}_i\cdot\hat{\mathbf{S}}_i\\ &= -\gamma_n\hbar\hat{\mathbf{I}}_i\cdot\left(\mathbf{H}_0 - \frac{\mathsf{A}_i\cdot\hat{\mathbf{S}}_i}{\gamma_n\hbar}\right)\\ &\equiv -\gamma_n\hbar\hat{\mathbf{I}}_i\cdot\hat{\mathbf{H}}_{eff,i}, \end{aligned} \tag{1}$$

where $\hat{\mathbf{I}}_i$ and $\hat{\mathbf{S}}_i$ are, respectively, the nuclear and electron spin operators at site i. We define $\hat{\mathbf{H}}_{eff,i}$ to be the effective field perceived by the nuclear spin at site i.

If the Zeeman term dominates the hyperfine interaction with the field applied along the axis α, then to first order the nuclear spin Hamiltonian is given by

$$\begin{aligned}\mathcal{H}_i &= -\gamma_n\hbar\hat{I}_i^{\alpha}\left(H_0 - \frac{1}{\gamma_n\hbar}(A_i^{\alpha a}S_i^a + A_i^{\alpha b}S_i^b + A_i^{\alpha c}S_i^c)\right)\\ &\equiv -\gamma_n\hbar\hat{I}_i^{\alpha}H_{eff,i}^{\alpha}, \end{aligned} \tag{2}$$

where we have replaced the electron spin operator $\hat{\mathbf{S}}$ with the thermal average expectation value $\mathbf{S}$.

As mentioned, there are four inequivalent dimer sites in the crystal, not including the inner-outer ^{13}C distinction. These sites can be related by the $\hat{\mathcal{G}}$ and $\hat{\mathcal{R}}$ symmetry operations, and thus the shift tensors of the different sites i can be related through the appropriate transformations. This is done in Appendix A.

Given the relations between the hyperfine tensors at each site, we can determine the electron spin configurations that will present a single resonance frequency: i.e., the spin configurations for which the effective field is the same at all four unit cell sites (since the effective field determines the resonance frequency through $\omega_i=\gamma_n H_{eff,i}$). This analysis is carried out with the understanding that the NMR data were taken in a field of 8.3 T, well above the spin-flop field. At fields below the spin-flop field the anisotropic exchange interaction wins out over the Zeeman interaction, pinning the spins along the easy axis $\hat{b}$. Above the spin-flop field, however, the Zeeman interaction is greater than the anisotropic exchange interaction, and assuming that the isotropic exchange interaction is much larger than the other interactions (supported by our data), the spins align in a direction roughly perpendicular to the external field (an alignment most advantageous for the Zeeman interaction), regardless of the spin orientation. The spins will also exhibit a slight canting toward the direction of the external field, as discussed later, but this can be ignored for the purposes of the analysis we are about to give.

As an example of how the analysis works, consider the case of $\mathbf{H}_0 \| \hat{a}$. Above the spin-flop field the spins will be oriented somewhere in the $\hat{b}$-$\hat{c}$ plane. If the spins are along $\hat{b}$, then we find the following effective fields at sites A1 and A2:

$$H_{eff,A1}=H_0-\frac{1}{\gamma_n\hbar}A^{ab}_{A1}S^{b}_{A1}, \tag{3}$$

while the effective field at A2 is

$$\begin{aligned} H_{eff,A2}&=H_0-\frac{1}{\gamma_n\hbar}A^{ab}_{A2}S^{b}_{A2} \\ &=H_0-\frac{1}{\gamma_n\hbar}A^{ab}_{A1}(-S^{b}_{A1}) \\ &=H_0+\frac{1}{\gamma_n\hbar}A^{ab}_{A1}S^{b}_{A1}, \end{aligned} \tag{4}$$

where we have used $A^{ab}_{A2}=A^{ab}_{A1}$ (from Appendix A) and $S^{b}_{A2}=-S^{b}_{A1}$ (antiferromagnetic alignment of neighboring spins). Thus $H_{eff,A1}\neq H_{eff,A2}$ and we would find two distinct resonance frequencies, contrary to our findings. Therefore, the electron spins cannot have a $\hat{b}$ component. Further analysis shows that the condition of a single effective field for the two sites can be satisfied if the electron spins lie along the $\hat{c}$ axis. Similar constraints hold for the ordering between the planes.

Carrying out this analysis with all possibilities for orientations of field and electron spins, we reach the following conclusions about the ordering of the electron spins for fields above the spin-flop field

(i) $\mathbf{H}_0 \| \hat{a}$. The spins are roughly oriented along the $\hat{c}$ axis (some small degree of canting will be present), a finding in agreement with Miyagawa *et al.*[20] In particular, $\mathbf{S}_{A1}\simeq -S\hat{c}$ and $\mathbf{S}_{A2}\simeq S\hat{c}$, where $|\mathbf{S}|=S$. We find that $\mathbf{S}_{A1}=\mathbf{S}_{B1}$ and $\mathbf{S}_{A2}=\mathbf{S}_{B2}$ so that there is ferromagnetic ordering between the planes. This ordering is depicted in Fig. 5.

(ii) $\mathbf{H}_0 \| \hat{b}$. The spins are along the $\hat{c}$ axis, again with $\mathbf{S}_{A1}\simeq -S\hat{c}$ and $\mathbf{S}_{A2}\simeq S\hat{c}$. For this field orientation, $\mathbf{S}_{A1}=-\mathbf{S}_{B1}$ and $\mathbf{S}_{A2}=-\mathbf{S}_{B2}$, giving antiferromagnetic ordering between planes. This is shown in Fig. 5.

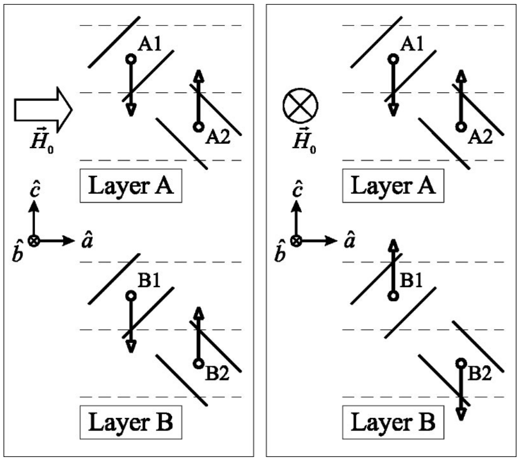

FIG. 5. Depiction of electron spin orderings for $\mathbf{H}_0 \| \hat{a}$ (left) and $\mathbf{H}_0 \| \hat{b}$ (right).

(iii) $\mathbf{H}_0 \| \hat{c}$. The spins can lie anywhere in the $\hat{a}$-$\hat{b}$ plane. There is ferromagnetic interplane ordering if the spins are along the $\hat{a}$ axis and antiferromagnetic ordering if the spins are along the $\hat{b}$ axis. The interplane ordering is more complicated for an arbitrary orientation of the spins in the $\hat{a}$-$\hat{b}$ plane.

Here interplane ordering is taken to be the relative ordering of A1 to B1 and A2 to B2—i.e., nearest neighbors across the polymer layer. Note that we have shown that the character of the interplane ordering changes with the orientation of the external field.

We do not include here a quantitative analysis of the line shifts in the magnetic state as Miyagawa *et al.*[20] have done for $\mathbf{H}_0 \| \hat{c}$, using the room-temperature hyperfine interaction tensors. While such an analysis provides a value for the dimer moment, we have found that the dimer moments thus found vary considerably from one orientation of the magnetic field to another. In addition, the values produced from the outer-site data are not consistent with those of the inner-site data. We suspect that the room-temperature hyperfine tensors may not apply in the magnetic state, with the inner tensor undergoing more of a change than the outer tensor. However, we note that our results show roughly a moment of $0.5\mu_B$ per dimer, consistent with the result of $0.4\mu_B$ per dimer found by Miyagawa *et al.*[17] This assumption of $0.5\mu_B$ per dimer will be used in the following analysis.

C. Model involving the DM interaction

Having determined the magnetic ordering of the system for fields above the spin-flop field, we now turn to understanding the cause of the ordering. The magnetization data suggest that a model for this system must minimally include an exchange term, a DM term (to account for the canting), an anisotropic exchange term (to account for the easy axis), and a Zeeman term. Such a spin Hamiltonian is the following:

$$\begin{aligned}\mathcal{H}_{spin}&=\mathcal{H}_{iso}+\mathcal{H}_{DM}+\mathcal{H}_{anis}+\mathcal{H}_{Zeeman}\\&=\frac{|J|}{2}\sum_{n,m}\hat{\mathbf{S}}_n\cdot\hat{\mathbf{S}}_m+\frac{1}{2}\sum_{n,m}\mathbf{D}_{nm}\cdot(\hat{\mathbf{S}}_n\times\hat{\mathbf{S}}_m)\\&\quad+\frac{\Delta J}{2}\sum_{n,m}\hat{S}_n^b\hat{S}_m^b+g\mu_B\mathbf{H}\cdot\sum_n\hat{\mathbf{S}}_n.\end{aligned}\tag{5}$$

Note that since the dimers should be spin $\frac{1}{2}$, we have chosen the anisotropy term to be anisotropic exchange between pairs of ions, rather than a lowest-order single-ion anisotropy term, which vanishes for spin $\frac{1}{2}$ (Ref. 29).

Using our microscopic spin Hamiltonian, Eq. (5), we can derive an expression for the macroscopic energy in terms of the magnetization vectors of the magnetic sublattices using a molecular-field approximation. We ignore the weaker interlayer exchange couplings and include only the nearest-neighbor intralayer couplings. The differences between the A and B layers necessitate separate terms for the two layers, so we use the subscript l to indicate the layer. The two magnetic sublattices are represented by the symbols $+$ and $-$, so that $+$ and $-$ will refer to lattice sites, not to spin orientations. Note that as shown in Fig. 4, sites 1, 3, 4, and 5 are associated with the $+$ sublattice and site 2 with the $-$ sublattice. However, as we will show, the ordering between layers is not fixed but depends on the orientation of the external field, so that the $+(-)$ sites in the A layer do not necessarily have the same orientation as the $+(-)$ sites in the B layer.

The resulting energy expression is

$$\begin{aligned}E=\sum_{l=A,B}&(2A\mathbf{M}_{+l}\cdot\mathbf{M}_{-l}+\mathbf{D}_l\cdot(\mathbf{M}_{+l}\times\mathbf{M}_{-l})\\&+2KM_{+l}^bM_{-l}^b-\mathbf{M}_{+l}\cdot\mathbf{H}_0-\mathbf{M}_{-l}\cdot\mathbf{H}_0).\end{aligned}\tag{6}$$

Here $\mathbf{M}_{+(-)l}$ represents the magnetization of the $+(-)$ sublattice at the layer l, A is the isotropic exchange parameter, and K is the anisotropic exchange parameter. The equations relating the microscopic parameters of Eq. (5) and the macroscopic parameters of Eq. (6) are provided in Appendix B.

In this form, we can show that symmetry of the system puts several constraints on the DM vectors, derived in Appendix C. From the intralayer symmetry (the glide operation) we obtain

$$D_l^c=0,\{l=A,B\},\tag{7}$$

and from the interlayer symmetry (the reflection operation) we obtain

$$D_B^a=-D_A^a,D_B^b=D_A^b.\tag{8}$$

From Eq. (7) it follows that

$$|\mathbf{D}_A|=\sqrt{(D_A^a)^2+(D_A^b)^2}.\tag{9}$$

Equation (8) shows that knowing $\mathbf{D}_A$, we know $\mathbf{D}_B$, and that $|\mathbf{D}_A|=|\mathbf{D}_B|$. We proceed using $\mathbf{D}_{12}$ (the interaction vector between sites A1 and A2) to represent the DM interaction at the microscopic level and $\mathbf{D}_A$ to represent the DM interaction at the macroscopic level.

As we will now show, the constraints on the DM vectors, Eqs. (7) and (8), are consistent with the magnetization data and provide an explanation for the unexpected NMR results. Starting with the latter, we first note that the NMR data were taken at 8.3 T, well above the spin-flop transition. As discussed earlier, in this regime the electron spins are nearly perpendicular to $\mathbf{H}_0$ and still largely antiparallel to each other, but there will be a slight canting toward $\mathbf{H}_0$ due to the influence of the Zeeman interaction.

Given this configuration, we propose that the DM term will determine the orientation of the spins in the plane perpendicular to the external field, with the anisotropic exchange having a negligible effect. We provide support for this assumption later, but now proceed with this assumption and describe an analysis of the electron spin orientations for the three directions of external field. Central to our reasoning is that the DM interaction favors canting of the electron moments in a plane perpendicular to the DM vector and that the DM vector is nonzero only for the $\hat{a}$ and $\hat{b}$ directions. To facilitate the explanation we introduce the staggered moment $\mathbf{M}_l^{\dagger}=(\mathbf{M}_{+l}-\mathbf{M}_{-l})/2$ and the ferromagnetic moment $\mathbf{M}_l^F=(\mathbf{M}_{+l}+\mathbf{M}_{-l})/2$. For antiferromagnetic ordering in the absence of any canting only the staggered moment will be present. A ferromagnet moment develops when canting is present.

(i) $\mathbf{H}_0\|\hat{a}$. Here the moments cant toward $\hat{a}$, so that $\mathbf{M}_l^F$ is along $\hat{a}$ and $\mathbf{M}_l^{\dagger}$ lies in the $\hat{b}$-$\hat{c}$ plane. Since $\mathbf{D}_l^c=0$, $\mathbf{M}_l^{\dagger}$ will be along $\hat{c}$ to take advantage of DM interaction through the nonzero $\mathbf{D}_l^b$. And since, from Eq. (8), $\mathbf{D}_A^b$ and $\mathbf{D}_B^b$ have the same sign, $\mathbf{M}_A^{\dagger}$ and $\mathbf{M}_B^{\dagger}$ will be parallel and ferromagnetic interplane ordering will occur.

(ii) $\mathbf{H}_0\|\hat{b}$. $\mathbf{M}_l^F$ is along $\hat{b}$ and $\mathbf{M}_l^{\dagger}$ is in the $\hat{a}$-$\hat{c}$ plane. Again, $\mathbf{M}_l^{\dagger}$ will be along $\hat{c}$ since $\mathbf{D}_l^c=0$ and $\mathbf{D}_l^a\neq 0$. In this case, however, $\mathbf{M}_A^{\dagger}$ and $\mathbf{M}_B^{\dagger}$ will be antiparallel as $\mathbf{D}_A^a$ and $\mathbf{D}_B^a$ have opposite signs, so that antiferromagnetic ordering interplane will occur.

(iii) $\mathbf{H}_0\|\hat{c}$. $\mathbf{M}_l^F$ is along $\hat{c}$ and $\mathbf{M}_l^{\dagger}$ is in the $\hat{a}$-$\hat{b}$ plane. Since the DM vector is also in the $\hat{a}$-$\hat{b}$ plane, the spins will lie in the $\hat{a}$-$\hat{b}$ plane in a direction perpendicular to the full DM vector.

The spin configurations that we have found to be energetically favorable for the DM interaction are the same as the experimentally determined configurations found in our discussion of the hyperfine tensors, allowing for the yet unresolved ambiguity in the orientation for $\mathbf{H}_0\|\hat{c}$. An important feature is that the DM interaction also explains the change in interlayer ordering from ferromagnetic to antiferromagnetic as we change the field orientation from $\hat{a}$ to $\hat{b}$. Thus the interlayer ordering is not determined by the interlayer exchange interaction, but by the external field and the intralayer DM interaction.

Having shown that our model gives a qualitative explanation of the NMR results, we will now apply it to the high-field magnetization data of Fig. 3. Using Eq. (6), we obtain the following result for the net magnetization in low temperatures and high fields (well above the spin-flop field):

TABLE I. Parameters determined by the high-field magnetization data of Fig. 3 fit with Eq. (10). Both microscopic (J, $\mathbf{D}_{12}$) and macroscopic (A, $\mathbf{D}_A$) parameters are given. A result of "-" indicates that the particular orientation of the magnetic field does not provide any information about that parameter.

	$\mathbf{H}_0 \| \hat{a}$	$\mathbf{H}_0 \| \hat{b}$	$\mathbf{H}_0 \| \hat{c}$
J (meV)	57 ± 3	43 ± 6	49 ± 2
$\|D_{12}^a\|$ ($\times 10^{-5}$ eV)	-	9.7 ± 0.5	-
$\|D_{12}^b\|$ ($\times 10^{-5}$ eV)	20 ± 2	-	-
$\|D_{12}^{ab}\|$ ($\times 10^{-5}$ eV)	-	-	32 ± 4
$A(\times 10^6)$	1.69 ± 0.08	1.3 ± 0.2	1.45 ± 0.06
$\|D_A^a\|$ ($\times 10^4$)	-	0.6 ± 0.3	-
$\|D_A^b\|$ ($\times 10^4$)	1.2 ± 0.1	-	-
$\|\mathbf{D}_A\|$ ($\times 10^4$)	-	-	1.9 ± 0.2

$$M^F(H_0) = \frac{|D_A^i| M_0 + H_0}{A}, \tag{10}$$

where for $\mathbf{H}_0 \| \hat{a}$, $|D_A^i| = |D_A^b|$, for $\mathbf{H}_0 \| \hat{b}$, $|D_A^i| = |D_A^a|$, and for $\mathbf{H}_0 \| \hat{c}$, $|D_A^i| = |\mathbf{D}_A|$, as explained above. In deriving this expression we have used $M^F = M_A^F + M_B^F$ and the fact that every dimer has four nearest neighbors in the plane. Based on our assumption of $0.5\mu_B$ per dimer, we use $M_0 = 1.45$ emu/cm^3.

From a linear fit to the high-field data of M^F vs $\mathbf{H}_0$ using Eq. (10) we obtain the results shown in Table I, presented in terms of both microscopic and macroscopic parameters. The values for $\mathbf{D}_{12}$ and $\mathbf{D}_A$ depend on our assumption of a magnetic moment of $0.5\mu_B$ per dimer, but the values for J and A do not.

We now present several arguments to suggest that the values shown in Table I are reasonable. First, from theory we expect to find that $D_{12}/J \approx \Delta g$ (Ref. 29). Indeed, our result of $|D_{12}^{ab}|/J = (6.6 \pm 0.7) \times 10^{-3}$ is of the same order of magnitude as the Δg values found by Kubota *et al.*,[30] $\Delta g \approx 5 \times 10^{-3}$. Second, note also that our measured susceptibilities are in the range of $\chi = (5.9–7.7) \times 10^{-7}$ emu/cm^3 or $(2.8–3.7) \times 10^{-4}$ emu/mol. These values are in agreement with the stated value of $\chi = 2.96 \times 10^{-4}$ emu/mol from Ohta *et al.*[31] Third, from Eq. (9) we can relate the three results for D_A. The data for $\mathbf{H}_0 \| \hat{c}$ provide us with a direct measurement of $|\mathbf{D}_A|$, giving $(1.9 \pm 0.2) \times 10^4$. From the data for $\mathbf{H}_0 \| \hat{a}$ and $\hat{b}$ we obtain $|\mathbf{D}_A| = \sqrt{(D_A^a)^2 + (D_A^b)^2} = (1.3 \pm 0.2) \times 10^4$. These two results do not differ greatly, and the discrepancy might be explained by the effects of the anisotropic interaction, which we ignored in deriving Eq. (10), or the uncertainty related to the large background signal $M_{background}$ that we subtracted out in obtaining the data of Fig. 3. Note that we cannot give a value for the magnitude of the microscopic parameter, $|\mathbf{D}_{12}|$, since at the microscopic level the $\hat{c}$ component is nonzero and we have no information on D_{12}^c. However, we do have a measurement of the projection of $\mathbf{D}_{12}$ into the $\hat{a}$-$\hat{b}$ plane, D_{12}^{ab}.

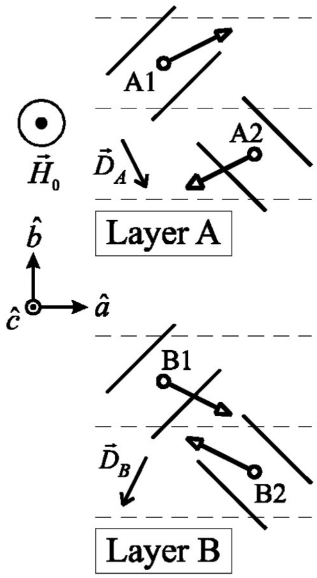

FIG. 6. Depiction of DM vectors and electron spin ordering for $\mathbf{H}_0 \| \hat{c}$.

With these values for the DM vector components there is enough information to describe the ordering of the electron spins for the case of $\mathbf{H}_0 \| \hat{c}$. In Appendix D we use the results of our NMR line shift analysis to show that D_A^a is positive, D_A^b is negative, D_B^a is negative, and D_B^b is negative. So $\mathbf{D}_A = (0.6\hat{a} - 1.2\hat{b}) \times 10^4$ and $\mathbf{D}_B = (-0.6\hat{a} - 1.2\hat{b}) \times 10^4$. Given that the spins will orient perpendicular to the DM vector in such a way that the canting toward $\hat{c}$ produces a cross product $\mathbf{M}_{+l} \times \mathbf{M}_{-l}$ in the direction opposite to the DM vector, the ordering will be as shown in Fig. 6.

The previous analysis rests on the assumption that the DM interaction is stronger than the anisotropic interaction. To support this claim we note without proof that our energy expression, Eq. (6), leads to the following expression for the spin-flop field:

$$H_{sf} = \frac{1}{4}\left[|D_A^a| + \sqrt{(D_A^a)^2 - 2(D_A^b)^2 + 16AK} \right]. \tag{11}$$

We have found that the spin-flop field is approximately 0.3 T. Using our results for D_A^a, D_A^b, and A from Table I we estimate that $K \approx 12$, a factor of 10^3 less than D_A. Thus our assumption that the anisotropic exchange interaction is much weaker than the DM interaction is self-consistent.

The model also helps to explain the torque magnetometry data of Pinterić *et al.*[18] They confirmed that the easy axis is along $\hat{b}$ and found that below the spin-flop transition the spins cant along $\hat{c}$ but not along $\hat{a}$. As they noted, this canting can be explained by a DM vector that has an $\hat{a}$ component but no $\hat{c}$ component. Considering the symmetry rules described by Moriya,[14] they focused on the interplane symmetry and showed that the interplane DM vector (the vector that describes the interaction between dimers on adjacent planes) must be in the $\hat{a}$-$\hat{c}$ plane. However, the interplane

DM vector is not constrained to be along $\hat{a}$, and the interplane DM interaction will be much weaker than the intraplane DM interaction, as the exchange coupling between planes is much weaker than the exchange coupling between adjacent dimers in the layer. Our symmetry analysis provides a stronger explanation for their results, as we have shown that in a molecular-field model the dominant intraplane DM vector does not have a $\hat{c}$ component.

Some preliminary analysis indicates that this model may also prove a success at describing the AFMR data of Ohta *et al.*[21,31]

V. CONCLUSION

We have provided a description of the electron spin ordering, above the spin-flop field, that is consistent with our NMR data. With the exception of $\mathbf{H}_0 \| \hat{c}$ the NMR data lead to an unambiguous assignment of ordering to the electron spins. We find the interesting result that the nature of the interlayer ordering depends on the direction of the applied magnetic field.

Based on an analysis of the symmetry, we have also described a model that explains the observed electron spin ordering. Central to the model is the DM interaction and the observation that crystal symmetry requires that the $\hat{c}$ component of the DM vector be zero between neighboring sites in the molecular-field approximation. Combined with the high-field magnetization results for the DM vector values (Table I), this model also allows us to remove the ambiguity in the $\mathbf{H}_0 \| \hat{c}$ ordering (Fig. 6).

From the high-field magnetization data we find values for the exchange interaction J of roughly 50 meV and for the DM interaction of roughly 0.3 meV. The latter result depends on our assumption of a moment of $0.5\mu_B$ per dimer. Finally, we find that our experimental value for the ratio $D/J \approx 3 \times 10^{-3}$ is approximately equal to $\Delta g \approx 5 \times 10^{-3}$ from electron spin resonance (ESR),[30] in agreement with the theoretical relation $\Delta g \approx D/J$.

ACKNOWLEDGMENTS

We would like to thank J.-P. Ansermet, T. Banks, A. Comment, S. L. Cooper, N. Curro, U. Geiser, J. Haase, A. Leggett, R. McKenzie, C. Milling, P. Molitor, B. Neils, K. Sakaie, R. Stern, R. Strange, V. Mainz, M.-H. Whangbo, and especially J. Schmalian, for helpful discussions. This work was supported by the U.S. Department of Energy, Division of Materials Sciences, through the Frederick Seitz Materials Research Laboratory at the University of Illinois at Urbana-Champaign under Award No. DEFG02-91ER45439 and through Argonne National Laboratory under Contract No. W-31-109-ENG-38.

APPENDIX A: HYPERFINE TENSOR SYMMETRY

We use the outer ^{13}C shift tensor at site A1 as our reference. Starting with the tensor as defined in the molecular basis, given in Sec. III A, we transform into the crystal basis to obtain

$$\mathsf{K}_{A1} = \begin{pmatrix} K_{A1}^{aa} & K_{A1}^{ab} & K_{A1}^{ac} \\ K_{A1}^{ba} & K_{A1}^{bb} & K_{A1}^{bc} \\ K_{A1}^{ca} & K_{A1}^{cb} & K_{A1}^{cc} \end{pmatrix} = \begin{pmatrix} 240.2 & 142.3 & 301.9 \\ 142.3 & 164.3 & 231.4 \\ 301.9 & 231.4 & 345.3 \end{pmatrix}, \tag{A1}$$

where the values are in ppm. Note that all of the components are positive. The $\hat{\mathcal{G}}$ operator takes A1 into A2 and B1 into B2, reflecting across the $\hat{a}$-$\hat{b}$ plane and changing the sign of the $\hat{c}$ components in the process. The $\hat{\mathcal{R}}$ operator reflects A1 with B1 and A2 with B2 in the $\hat{a}$-$\hat{c}$ plane, changing the sign of the $\hat{b}$ components. The resulting tensors are as follows:

$$\mathsf{K}_{A2} = \begin{pmatrix} 240.2 & 142.3 & -301.9 \\ 142.3 & 164.3 & -231.4 \\ -301.9 & -231.4 & 345.3 \end{pmatrix}, \tag{A2}$$

$$\mathsf{K}_{B1} = \begin{pmatrix} 240.2 & -142.3 & 301.9 \\ -142.3 & 164.3 & -231.4 \\ 301.9 & -231.4 & 345.3 \end{pmatrix}, \tag{A3}$$

$$\mathsf{K}_{B2} = \begin{pmatrix} 240.2 & -142.3 & -301.9 \\ -142.3 & 164.3 & 231.4 \\ -301.9 & 231.4 & 345.3 \end{pmatrix}. \tag{A4}$$

APPENDIX B: RELATING MICROSCOPIC AND MACROSCOPIC PARAMETERS

Here we present the relations that allow us to convert from microscopic parameters (J, ΔJ, $\mathbf{D}_{12}$, $\mathbf{S}$) to the macroscopic parameters (A, K, $\mathbf{D}$, $\mathbf{M}$). In these equations $n_u \approx 3.1 \times 10^{20}$ cm^{-3} is the density of unit cells and $Z=4$ is the number of nearest neighbors:

$$\mathbf{M}_{+(-)l} = -n_u g \mu_B \mathbf{S}_{+(-)l}, \tag{B1}$$

$$A = \frac{Z}{2(g\mu_B)^2 n_u} J, \tag{B2}$$

$$K = \frac{Z}{2(g\mu_B)^2 n_u} \Delta J, \tag{B3}$$

$$|D_l^i| = \frac{4}{(g\mu_B)^2 n_u} |D_{12}^i|. \tag{B4}$$

APPENDIX C: DM VECTOR SYMMETRY

In this appendix we begin with the symmetry analysis of the DM vector at the level of the macroscopic molecular-field energy of Eq. (6). While this analysis relies on the molecular-field approximation, it brings us directly to the constraints on the macroscopic DM vector. A similar analysis can be carried out at the microscopic level of Eq. (5), making no assumptions about the nature of the ordering. These microscopic results are consistent with the macroscopic results, and while the analysis will not be shown, the resulting constraints are presented in the final section of this appendix.

1. Glide operator $\hat{\mathcal{G}}$

For the analysis of the macroscopic DM vector, we begin with the glide operator $\hat{\mathcal{G}}$, which takes the $+$ sublattice of a given plane into the $-$ sublattice of the same plane. Since $\hat{\mathcal{G}}$ involves a reflection in the $\hat{a}$-$\hat{b}$ plane and the spins (and therefore magnetization vectors) are pseudovectors, the $\hat{a}$ and $\hat{b}$ components of the spins change sign under the glide, but the $\hat{c}$ component does not (in contrast to the effect of $\hat{\mathcal{G}}$ on a vector, for which only the $\hat{c}$ components would change sign). This analysis holds for both the A and B layers, so we have omitted the subscript l below.

The DM interaction between $\mathbf{M}_+$ and $\mathbf{M}_-$ is

$$\begin{aligned}E_{DM}&=\mathbf{D}\cdot(\mathbf{M}_+\times\mathbf{M}_-)\\&=\mathbf{D}\cdot[(M_+^a,M_+^b,M_+^c)\times(M_-^a,M_-^b,M_-^c)]\\&=D^a(M_+^bM_-^c-M_+^cM_-^b)+D^b(M_+^cM_-^a-M_+^aM_-^c)\\&\quad+D^c(M_+^aM_-^b-M_+^bM_-^a).\end{aligned}\tag{C1}$$

After applying $\hat{\mathcal{G}}$ we obtain

$$\begin{aligned}E'_{DM}&=\mathbf{D}\cdot(\mathbf{M}'_-\times\mathbf{M}'_+)\\&=\mathbf{D}\cdot[(-M_-^a,-M_-^b,M_-^c)\times(-M_+^a,-M_+^b,M_+^c)]\\&=D^a(M_+^bM_-^c-M_+^cM_-^b)+D^b(M_+^cM_-^a-M_+^aM_-^c)\\&\quad-D^c(M_+^aM_-^b-M_+^bM_-^a).\end{aligned}\tag{C2}$$

The invariance of the energy under $\hat{\mathcal{G}}$ implies that the DM interaction between these two independent spins will also be invariant under the transformation. Thus $E_{DM}=E'_{DM}$ which implies that

$$D^c=0.\tag{C3}$$

2. Reflection operator $\hat{\mathcal{R}}$

$\hat{\mathcal{R}}$ reflects the system in the $\hat{a}$-$\hat{c}$ plane. We consider two pairs of sites related by such a reflection, sites A1 and A2 in the A layer and sites B1 and B2 in the B layer, as in Fig. 4. Sites 1 and 2 represent the $+$ and $-$ sublattices, respectively.

The DM interaction involving these four spins is

$$\begin{aligned}E_{DM,AB}&=\mathbf{D}_A\cdot(\mathbf{M}_{A+}\times\mathbf{M}_{A-})+\mathbf{D}_B\cdot(\mathbf{M}_{B+}\times\mathbf{M}_{B-})\\&=\mathbf{D}_A\cdot[(M_{A+}^a,M_{A+}^b,M_{A+}^c)\times(M_{A-}^a,M_{A-}^b,M_{A-}^c)]\\&\quad+\mathbf{D}_B\cdot[(M_{B+}^a,M_{B+}^b,M_{B+}^c)\\&\quad\times(M_{B-}^a,M_{B-}^b,M_{B-}^c)].\end{aligned}\tag{C4}$$

$\hat{\mathcal{R}}$ exchanges $\mathbf{M}_{A+}$ with $\mathbf{M}_{B+}$ and exchanges $\mathbf{M}_{A-}$ with $\mathbf{M}_{B-}$. The reflection also changes the sign of the $\hat{a}$ and $\hat{c}$ components of the magnetizations. The transformed expression is

$$\begin{aligned}E'_{DM,AB}=\mathbf{D}_A\cdot[&(-M_{B+}^a,M_{B+}^b,-M_{B+}^c)\\&\times(-M_{B-}^a,M_{B-}^b,-M_{B-}^c)]\\&+\mathbf{D}_B\cdot[(-M_{A+}^a,M_{A+}^b,-M_{A+}^c)\\&\times(-M_{A-}^a,M_{A-}^b,-M_{A-}^c)].\end{aligned}\tag{C5}$$

Equating the coefficients of the cross products of $E_{DM,AB}$ and $E'_{DM,AB}$ we find

$$D_B^a=-D_A^a,D_B^b=D_A^b,D_B^c=-D_A^c.\tag{C6}$$

3. Microscopic results

Here we present the constraints on the microscopic DM vectors. From $\hat{\mathcal{G}}$ we find

$$D_{23}^a=-D_{12}^a,D_{23}^b=-D_{12}^b,D_{23}^c=D_{12}^c.\tag{C7}$$

From the inversion operator, $\hat{\mathcal{I}}$, we find

$$\mathbf{D}_{25}=-\mathbf{D}_{12},\mathbf{D}_{42}=-\mathbf{D}_{23}.\tag{C8}$$

Finally, from $\hat{\mathcal{R}}$ we find

$$\begin{aligned}D_{B1,B2}^a&=-D_{A1,A2}^a,\\D_{B1,B2}^b&=D_{A1,A2}^b,\\D_{B1,B2}^c&=-D_{A1,A2}^c.\end{aligned}\tag{C9}$$

When taken in the context of the molecular-field approximation, these constraints provide the same information as the analysis found in the previous two sections of this appendix.

APPENDIX D: THE SIGNS OF THE DM VECTOR COMPONENTS

Consider separately the cases of $\mathbf{H}_0\|\hat{a}$ and $\mathbf{H}_0\|\hat{b}$.

(i) $\mathbf{H}_0\|\hat{a}$. We have seen that for this orientation our analysis of the NMR data requires that $\mathbf{S}_{A1}\simeq-S\hat{c}$ and $\mathbf{S}_{A2}\simeq+S\hat{c}$ (Fig. 5). We know that this ordering is such as to minimize the DM interaction, and since the spins are canting toward $-\hat{a}$ due to the Zeeman interaction, the cross product $\mathbf{S}_{A1}\times\mathbf{S}_{A2}$ will be along the $+\hat{b}$ axis. The $\hat{b}$ component of the DM vector, D_{12}^b, must therefore be negative for the DM interaction $\mathbf{D}_{A1,A2}\cdot(\mathbf{S}_{A1}\times\mathbf{S}_{A2})$ to be negative. Relating site A1 to the $+$ magnetic sublattice and site A2 to the $-$ magnetic sublattice, we find it is also true in the molecular-field formulation that D_A^b is negative. Equation (C6) then tells us that D_B^b is also negative.

(ii) $\mathbf{H}_0 \| \hat{b}$. For this orientation of the external field we found that $\mathbf{S}_{A1} \simeq -S\hat{c}$ and $\mathbf{S}_{A2} \simeq +S\hat{c}$, as shown in Fig. 5. Given canting toward $-\hat{b}$ due to the external field, the cross product $\mathbf{S}_{A1} \times \mathbf{S}_{A2}$ will be along the $-\hat{a}$ axis and therefore the $\hat{a}$ component of the DM vector, D_{12}^a, must be positive. It follows that D_A^a is positive and, from Eq. (C6), D_B^a is negative.

---

*Electronic address: dfsmith@uiuc.edu

†Now at Texas Instruments (Dallas).

[1] A.M. Kini *et al.*, Inorg. Chem. **29**, 2555 (1990).

[2] J.M. Williams *et al.*, Inorg. Chem. **29**, 3272 (1990).

[3] H.H. Wang *et al.*, Synth. Met. **41-43**, 1983 (1991).

[4] R.H. McKenzie, Comments Condens. Matter Phys. **18**, 309 (1998).

[5] J. Wosnitza, J. Low Temp. Phys. **117**, 1701 (1999).

[6] S.M. De Soto, C.P. Slichter, H.H. Wang, U. Geiser, and J.M. Williams, Phys. Rev. Lett. **70**, 2956 (1993).

[7] H. Mayaffre, P. Wzietek, C. Lenoir, D. Jérome, and P. Batail, Europhys. Lett. **28**, 205 (1994).

[8] R.H. McKenzie, Science **278**, 820 (1997).

[9] J. Schmalian, Phys. Rev. Lett. **81**, 4232 (1998).

[10] H. Kino and H. Kontani, J. Phys. Soc. Jpn. **67**, 3691 (1998).

[11] H. Kondo and T. Moriya, J. Phys. Soc. Jpn. **67**, 3695 (1998).

[12] K. Kuroki, T. Kimura, R. Arita, Y. Tanaka, and Y. Matsuda, Phys. Rev. B **65**, 100516(R) (2002).

[13] I.E. Dzialoshinskii, Sov. Phys. JETP **5**, 1259 (1957).

[14] T. Moriya, Phys. Rev. **120**, 91 (1960).

[15] D. Coffey, K.S. Bedell, and S.A. Trugman, Phys. Rev. B **42**, 6509 (1990).

[16] U. Welp, S. Fleshler, W.K. Kwok, G.W. Crabtree, K.D. Carlson, H.H. Wang, U. Geiser, J.M. Williams, and V.M. Hitsman, Phys. Rev. Lett. **69**, 840 (1992).

[17] K. Miyagawa, A. Kawamoto, Y. Nakazawa, and K. Kanoda, Phys. Rev. Lett. **75**, 1174 (1995).

[18] M. Pinterić, M. Miljak, N. Biskup, O. Milat, I. Aviani, S. Tomić, D. Schweitzer, W. Strunz, and I. Heinen, Eur. Phys. J. B **11**, 217 (1999).

[19] K. Kanoda, Physica C **282-287**, 299 (1997).

[20] K. Miyagawa, A. Kawamoto, and K. Kanoda, Phys. Rev. Lett. **89**, 017003 (2002).

[21] H. Ohta, N. Nakagawa, K. Akioka, Y. Nakashima, S. Okubo, K. Kanoda, and N. Kitamura, Synth. Met. **103**, 1914 (1999).

[22] H. Ito, G. Saito, and T. Ishiguro, J. Phys. Chem. Solids **62**, 109 (2001).

[23] The notation $\kappa\text{-}(^{13}\mathrm{C}_n\text{-ET})_2\mathrm{Cu}[\mathrm{N(CN)}_2]\mathrm{Cl}$ is used to indicate a sample of $\kappa\text{-}(\mathrm{ET})_2\mathrm{Cu}[\mathrm{N(CN)}_2]\mathrm{Cl}$ with a number n of the carbons labeled with $^{13}\mathrm{C}$ in each ET molecule.

[24] S.M. De Soto, C.P. Slichter, A.M. Kini, H.H. Wang, U. Geiser, and J.M. Williams, Phys. Rev. B **52**, 10 364 (1995).

[25] The $\kappa\text{-}(^{13}\mathrm{C}_6\text{-ET})_2\mathrm{Cu}[\mathrm{N(CN)}_2]\mathrm{Cl}$ compound contains six $^{13}\mathrm{C}$ isotopes per molecule. Two $^{13}\mathrm{C}$ isotopes are present at the two "central" sites, as for $\kappa\text{-}(^{13}\mathrm{C}_2\text{-ET})_2\mathrm{Cu}[\mathrm{N(CN)}_2]\mathrm{Cl}$. In addition, the next four C sites, moving outward from the center of the molecule, are labeled with $^{13}\mathrm{C}$. In Geiser *et al.* (Ref. 32), these are the carbons denoted by C3, C4, C5, and C6. We used this crystal in the magnetometry experiments simply because of its large size, not because of its isotopic labeling.

[26] S.M. De Soto, D.F. Smith, and C.P. Slichter, Bull. Am. Phys. Soc. **41**, 71 (1996).

[27] A. Kawamoto, K. Miyagawa, Y. Nakazawa, and K. Kanoda, Phys. Rev. B **52**, 15 522 (1995).

[28] Windle, *A First Course in Crystallography* (Bell, London, 1977).

[29] K. Yosida, *Theory of Magnetism* (Springer-Verlag, Berlin, 1996).

[30] M. Kubota, G. Saito, H. Ito, T. Ishiguro, and N. Kojima, Mol. Cryst. Liq. Cryst. Sci. Technol., Sect. A **284**, 367 (1996).

[31] H. Ohta, S. Kimura, Y. Yamamoto, J. Azuma, K. Akioka, M. Motokawa, and K. Kanoda, Synth. Met. **86**, 2079 (1997).

[32] U. Geiser *et al.*, Physica C **174**, 475 (1991).